Designing breathing air-electrode and enhancing the oxygen electrocatalysis by thermoelectric effect for efficient Zn-air batteries

Xuerong Zheng
Tianjin University   https://orcid.org/0000-0002-0161-4077

Yanhui Cao
Tianjin University

Xiaopeng Han
Tianjin University   https://orcid.org/0000-0002-7557-7133

Haozhi Wang
Tianjin University

Zhao Zhang
Tianjin University

Menghan Zhao
Tianjin University

Jihong Li
Hainan University

Yang Wang
Tianjin University

Jiajun Wang
Tianjin University

Yuesheng Wang (✉ Yueshengwang1@gmail.com)
Hydro-Québec   https://orcid.org/0000-0001-7269-9015

Li Zhang
Shaanxi University of Science & Technology

Karim Zaghib
Concordia University

Yida Deng
Tianjin University

Wenbin Hu
Tianjin University

Article

Designing breathing air-electrode and enhancing the oxygen electrocatalysis by thermoelectric effect for efficient Zn-air batteries

Xuerong Zheng[1,2,6], Yanhui Cao[2,6], Xiaopeng Han[2], Haozhi Wang[1], Zhao Zhang[2], Menghan Zhao[2], Jihong Li[1], Yang Wang[1], Jiajun Wang[2], Yuesheng Wang[3*], Li Zhang[4], Zaghib Karim[5], Yida Deng[1,2*], Wenbin Hu[2]*

[1]State Key Laboratory of Marine Resource Utilization in South China Sea, School of Materials Science and Engineering, Hainan University, Haikou 570228, P. R. China.

[2]Key Laboratory of Advanced Ceramics and Machining Technology of Ministry of Education, School of Materials Science and Engineering, Tianjin University, Tianjin 300072, P. R. China.

[3]Center of Excellence in Transportation Electrification and Energy Storage, Hydro-Quebec, 1806 boulevard Lionel-boulet, Varennes, Quebec J3X 1S1, Canada

[4]School of Materials Science and Engineering, Shaanxi University of Science & Technology, Xi'an 710021, China

[5]Department of Chemical and Materials Engineering, Concordia University, Montréal, 510610, Canada

[6]These authors contributed equally: Xuerong Zheng, Yanhui Cao.

Email: xphan@tju.edu.cn; wys_shuicheng@163.com; yida.deng@tju.edu.cn

ABSTRACT:

The sluggish kinetics and mutual interference of oxygen evolution and reduction reactions (OER and ORR) in the air electrode resulted in large charge/discharge overpotential and low energy efficiency of Zn-air batteries. In this work, we designed a breathing air-electrode configuration in Zn-air batteries using P-type $Ca_3Co_4O_9$ and N-type $CaMnO_3$ as charge and discharge thermoelectrocatalysts, respectively. The Seebeck voltages generated from thermoelectric effect of $Ca_3Co_4O_9$ and $CaMnO_3$ synergistically compensated the OER and ORR overpotentials. The carrier migration and accumulation on the cold surface of $Ca_3Co_4O_9$ and $CaMnO_3$ optimized the electronic structure of metallic sites and thus enhanced their intrinsic catalytic activity. The OER and ORR overpotentials were enhanced by 101 and 90 mV, respectively, at temperature gradient of 200 °C. The breathing Zn-air battery displayed a remarkable energy efficiency of 68.1%. This work provides an efficient avenue towards utilizing waste heat for improving the energy efficiency of Zn-air batteries.

Introduction.

Rechargeable Zn-air batteries (ZABs) are frequently advocated as next-generation electrochemical energy storage systems due to the advantages regarding high energy density, inherent safety, and affordability.[1-4] However, the large charge/discharge overpotentials and low round-trip energy efficiency stand in the way for their practical application.[3,5] These issues are mainly caused by the multi-electron processes and the as-resulted sluggish catalytic kinetics of oxygen evolution and reduction reactions (OER and ORR) for charging and discharging, respectively.[6-8] To address these issues, nano-engineering strategies, such as constructing microstructures, introducing defects and interfaces, were performed to regulate the electronic and local coordinated structure of metallic sites to enhance their intrinsic catalytic activity.[4,9-11] However, due to the reverse OER and ORR have different requirements for the property of active sites, the bifunctional activity of the catalysts is difficult to be enhanced simultaneously. It is also difficult to separately tune the OER and ORR process because both the two reactions are integrated within one air electrode. Moreover, some ORR catalytic sites would be inevitably damaged due to the exposure to the harsh OER oxidative potential, which usually triggers irreversible surface reconstruction. In addition, the repeated reductive-oxidative reactions that occur in the air electrode during battery cycling would also deactivate the ORR active component. [12-16]

Introducing external field, such as magnetic, electric, and light field, was regarded as extremely promising strategy for improving the intrinsic activity of the electrocatalysts. [17-19] Thermoelectric devices and rechargeable ZABs are two totally different energy conversion and storage systems for electricity utilization. The former can convert thermal gradient into electricity but cannot store it for long-term utilization, while the latter can store and supply electricity with outstanding cycling stability via OER and ORR processes for charging and discharging, respectively. [20-21] Therefore, integrating the two systems together would result in synergism of their energy storage properties. As previous reported,[22] the thermoelectric materials of Sb_2Te_3 and $Bi_{0.5}Sb_{1.5}Te_3$ could function as electrocatalysts and the generated thermoelectric voltages could potentially promote HER activity. However, limited study has been performed to enhance the OER
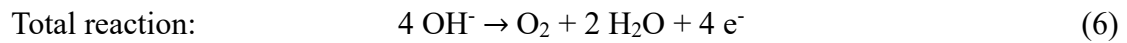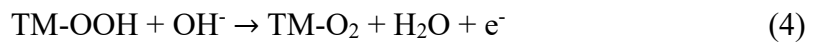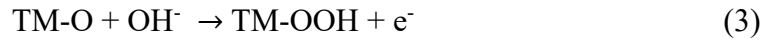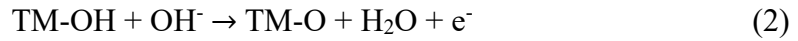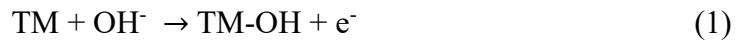
and ORR activities and to compensate the charging/discharging potentials through thermoelectric effect. Theoretically, on one hand, thermoelectric materials functioning as electrocatalysts can provide thermoelectric voltage to initiate and boost electrocatalytic reactions under temperature gradients. On the other hand, the thermoelectric devices with parallel arrayed P-type and N-type legs can provide preferable opportunity to separately and simultaneously enhance the OER and ORR properties. As a matter of fact, it is critical but highly challenging to put the concept into practice for developing thermoelectric enhanced ZAB systems.

In this work, we successfully integrated the thermoelectric and ZAB into one system by constructing a breathing Zn-air battery using the P-type $Ca_3Co_4O_9$ and N-type $CaMnO_3$ thermoelectrocatalysts as charging and discharging electrodes, respectively. In the air-electrode configuration, the $Ca_3Co_4O_9$ and $CaMnO_3$ were physically decoupled but connected in series on the heating plate, so that their Seebeck voltages generated from thermoelectric effect can synergistically compensate a part of charging overpotential. Moreover, the energy band and electronic structure of thermoelectrocatalysts were optimized due to the accumulation of thermoelectric generated carriers (h^- for $Ca_3Co_4O_9$ and e^- for $CaMnO_3$) on the cold surface of catalysts upon thermal gradient, thus enhancing the intrinsic catalytic activity of metallic sites. The OER overpotential (10 mA cm^{-2}) and ORR on-set potential were optimized from 407 mV to 306 mV and from 0.72 V to 0.81 V, respectively, with the ΔT values increased from 0 to 200 °C. The charge/discharge potential gap of the breathing Zn-air battery was decreased from 0.86 V to 0.63 V, and the energy efficiency was increased from 58.6% to 68.1%. This work provides an efficient, cost-effective, and eco-friendly avenue towards utilizing waste heat for exploring high energy efficient metal-air battery systems.
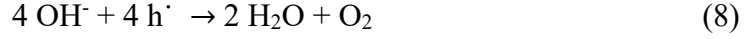
Results.

Mechanism of the breathing zinc–air battery. Thermoelectrocatalysts play critical role for not only act as thermoelectric materials to generate electricity under proper temperature gradient, but also as electrocatalysts to boost catalytic reactions such as

OER and ORR. To efficiently generate and utilize the thermoelectric energy, the thermoelectrocatalysts need to meet some specific requirements: (i) provide sufficient voltage to promote the electrochemical reactions; (ii) efficient catalytic center to boost the electrochemical reactions. Based on these pre-requisites, $CaMnO_3$ and $Ca_3Co_4O_9$ are ideal candidates to be employed as P- and N-type thermoelectrocatalysts. Fig. 1a schematically illustrates the basic structure and working mechanism of the breathing ZAB, which contains physically decoupled but bi-air-electrode system that is connected in series. For charging (Fig. 1b), the switching valve of the power source connected to the $CaMnO_3$ electrode. The thermoelectric Seebeck voltages ($\Delta V = V_1 + V_2$, $V_1 = E_2 - E_1$, $V_2 = E_4 - E_3$) generated from $Ca_3Co_4O_9$ and $CaMnO_3$ were in the same direction and synergistically compensate part of the OER overpotential. Moreover, the thermoelectric effect of the air electrode configuration is proposed to change the OER mechanism and accelerate the oxygen evolution process in charging process. The conventional OER mechanism should come down to the following equations (Eq. 1-6) steps:

$$TM + OH^- \rightarrow TM\text{-}OH + e^- \tag{1}$$

$$TM\text{-}OH + OH^- \rightarrow TM\text{-}O + H_2O + e^- \tag{2}$$

$$TM\text{-}O + OH^- \rightarrow TM\text{-}OOH + e^- \tag{3}$$

$$TM\text{-}OOH + OH^- \rightarrow TM\text{-}O_2 + H_2O + e^- \tag{4}$$

$$TM\text{-}O_2 \rightarrow TM + O_2 \tag{5}$$

Total reaction: $$4\ OH^- \rightarrow O_2 + 2\ H_2O + 4\ e^- \tag{6}$$

The four-step reactions involve chemisorption/desorption of oxygen-containing species and electron transfer, resulting in the sluggish OER kinetics. However, in the breathing ZAB, the oxidation process on cathode $Ca_3Co_4O_9$ and reduction process on anode Zn was enhanced. During charging, the thermoelectric generated electrons in $CaMnO_3$ would transfer from hot side to cold side and further to the Zn anode through external circuit, thus reducing Zn^{2+} to Zn (Eq. 7). The thermoelectric generated holes in $Ca_3Co_4O_9$ simultaneously migrate to the cold surface and oxidizing alkaline electrolyte to oxygen (Eq. 8). The anode and cathode reactions for charging of the breathing ZAB are illustrated in Eq. 7-9:

$$Zn(OH)_4^{2-} + 2\ e^- = Zn + 4\ OH^- \tag{7}$$

$$4\ OH^- + 4\ h^{\cdot} \rightarrow 2\ H_2O + O_2 \tag{8}$$

$$Co^{3+} + h^{\cdot} \rightarrow Co^{3+\delta} \tag{9}$$

This mechanism can reduce the charge potential of ZABs through the accelerated redox reactions on both cathode and anode. The accumulated holes on the surface of $Ca_3Co_4O_9$ would not only cause strong oxidation reaction to facilitate the OER reaction, but also oxidize the Co^{3+} ions to high valence state to enhance their intrinsic catalytic activity (Eq. 9). Moreover, thermoelectric voltages generated from both P-type and N-type electrodes in the bi-air-electrode configuration could synergistically compensate the OER overpotential. In the same way, for discharging the breathing ZABs, the ORR potential could be compensated and the intrinsic catalytic activity could be enhanced due to the thermoelectric effect in the bi-air-electrode configuration. The thermoelectric generated e^- would accumulate on the cold surface of N-type cathode, while the thermoelectric generated $h^{\cdot}$ would transfer from hot side to cold side of P-type cathode and further transfer from external circuit to the anode. The electrode reactions are proposed as Eq. 10-11:

$$Zn + 4\ OH^- = Zn(OH)_4^{2-} + 2\ e^- \tag{10}$$

$$4\ e^- + O_2 + 2\ H_2O \rightarrow 4\ OH^- \tag{11}$$
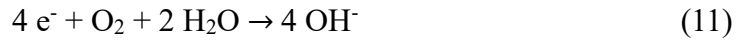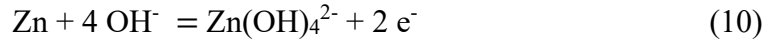
For discharging (Fig. 1c), the ORR process occurred on the surface of $CaMnO_3$ electrode. The thermoelectric generated electrons could directly reduce O_2 into OH^- in the electrolyte which is much faster than the traditional four-step ORR reaction. Moreover, the thermoelectric generated holes migrate to the anode through external circuit, thus compensating part of ORR overpotential. Based on the above discussion, the synergistic effect of N- and P-type thermoelectrocatalysts in the bi-air-electrode configuration can significantly enhance the charge and discharge performance of the ZABs through the following factors: (1) The thermoelectric Seebeck voltages generated from $Ca_3Co_4O_9$ and $CaMnO_3$ could compensate part of OER/ORR overpotential; (2) The migration of thermoelectric generated holes and electrons from hot to cold surface of electrodes could modify the electronic state of metallic sites which may enhance

their intrinsic catalytic activity for OER/ORR. The next consideration is how to put this concept into practice.
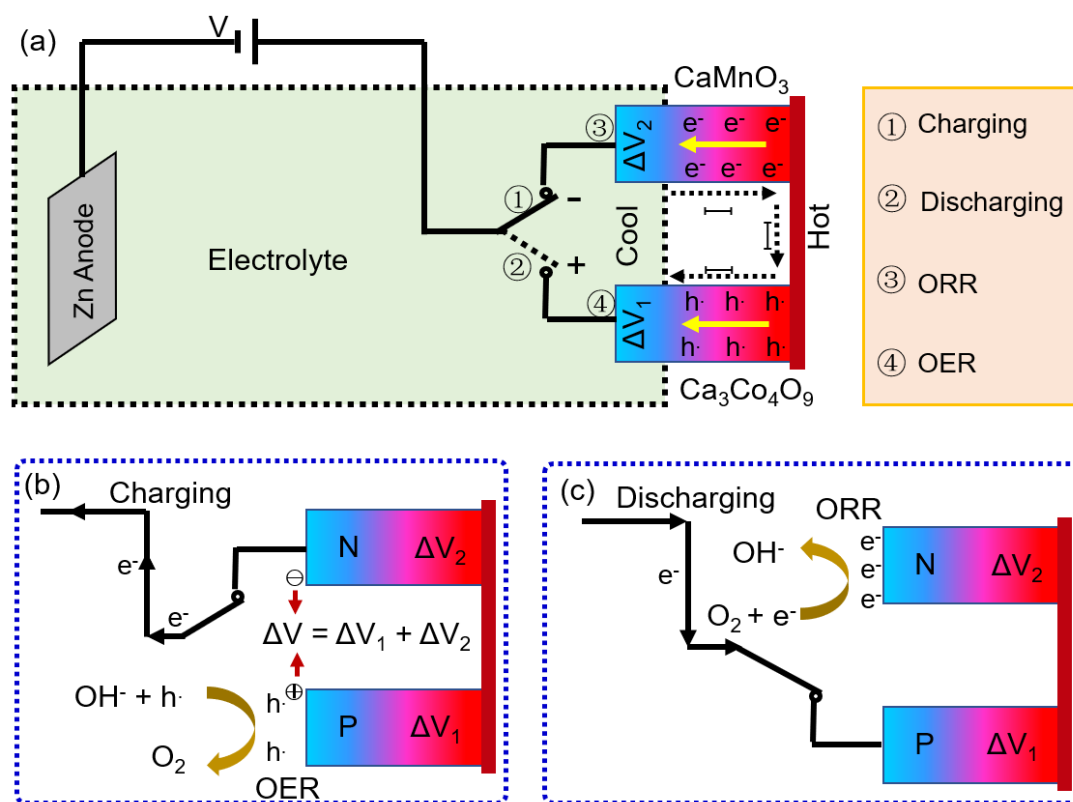

Fig. 1 Designing mechanism of breathing ZABs. **a** Schematic illustration of the breathing ZAB with thermoelectric-promoted air-breathing configuration. The detail illustration of **b** charging and **c** discharging process in the air-breathing configuration.

Characterizations of thermoelectrocatalysts. The P-type $Ca_3Co_4O_9$ and N-type $CaMnO_3$ were synthesized by sol-gel method (detailed method is shown in Supporting information). The Rietveld-refined X-ray diffraction (XRD) patterns of $CaMnO_3$ (JCPDS:50-1746) and $Ca_3Co_4O_9$ (JCPDS: 23-0110), and the crystal structure are shown in Fig. 2a and Supplementary Table 1. $CaMnO_3$ has a cubic perovskite structure in which the Mn^{4+} stand in the corner-shared octahedra ($MnO_{6/2}$) and Ca^{2+} located at the center of the 12-fold coordinated sites. $Ca_3Co_4O_9$ possesses a hybrid lattice structure in which the CdI_2-type $[CoO_2]$ layer and the $[Ca_2CoO_3]$ layer commensurately stacked alternately along the c-axis. The particle size of $CaMnO_3$ is about 100 nm with narrow size-distribution, and the Ca, Mn, and O elements are evenly distributed in the particles

as shown in the elemental mapping images (Supplementary Fig. 1). The exposed facet and crystallographic characteristics of $CaMnO_3$ are revealed by the high-angle annular dark-field scanning transmission electron microscopy (HAADF-STEM) image and the corresponding fast Fourier transform (FFT) in Fig. 2b. The high resolution XPS spectra of Ca, Mn, and O elements for $CaMnO_3$ are shown in Supplementary Fig. 2. The $Ca_3Co_4O_9$ particles are in the range of 100-200 nm, and the Ca, Co, and O elements are uniformly distributed in the particles (Supplementary Fig. 3). The polyhedral morphology of $Ca_3Co_4O_9$ should be determined by its structural feature. The HAADF-STEM image of $Ca_3Co_4O_9$ (Fig. 2c) shows obvious mis-fit between adjacent layers. The distorted lattice structure should be caused by the mismatch between rock salt $[Ca_2CoO_3]$ and hexagonal $[CoO_2]$ layers as reported in related references.[23] Both the layers of $[Ca_2CoO_3]$ and $[CoO_2]$ have the same a, c and β lattice parameters but different b parameters. The atomic level HAADF-STEM image and the fitted results, as well as the lattice atomic arrangement model (Supplementary Fig. 3b), revealed the incommensurate layered structure that alternately stacked by the $[Ca_2CoO_3]$ layers (consisting of CaO-CoO-CaO) and $[CoO_2]$ layer along the c axis.[24] The XPS spectra of Ca 2p, Co 2p, and O 1s are shown in Supplementary Fig. 4.
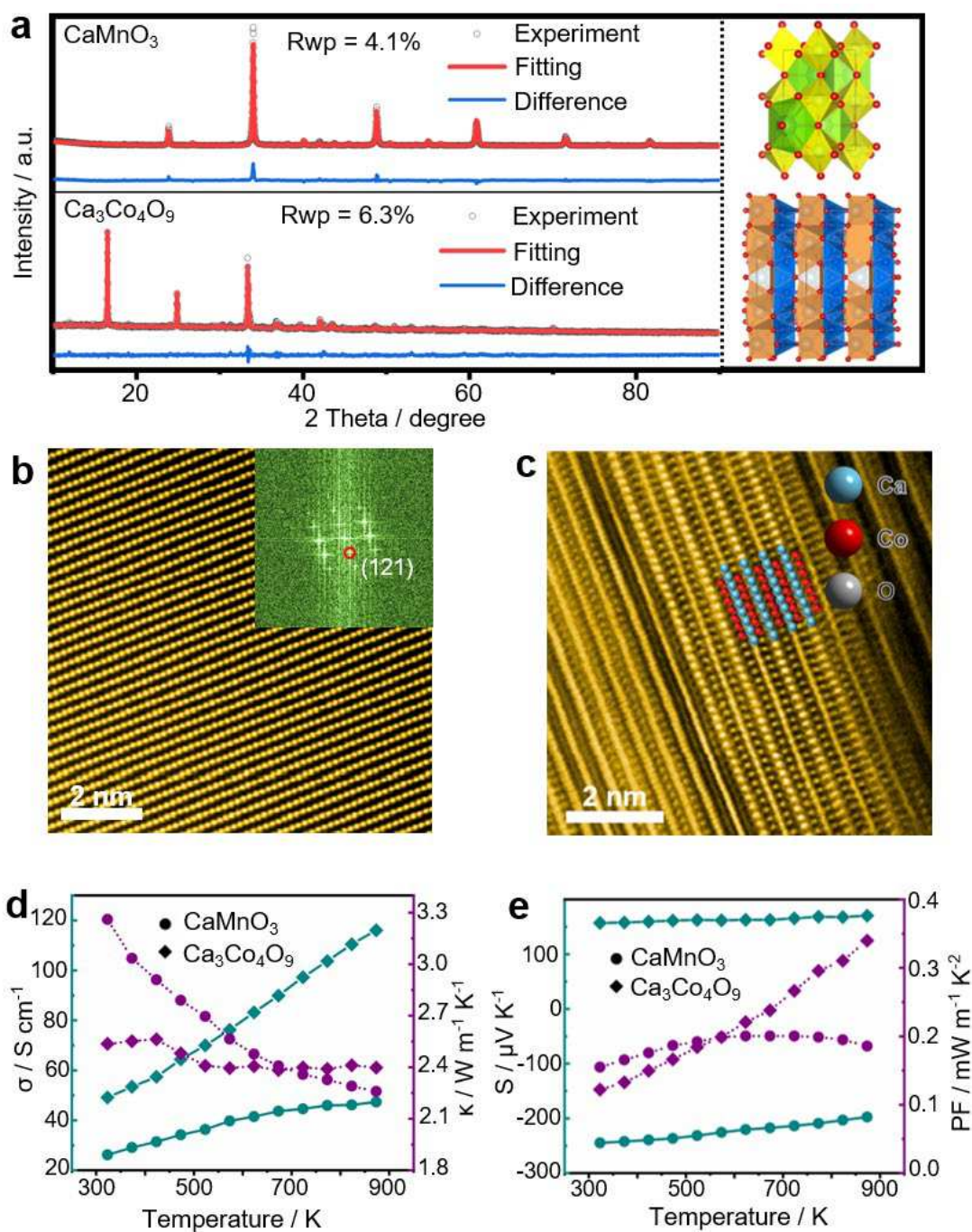
Fig. 2 Characterizations of thermoelectrocatalysts. **A** Characterized, calculated, and fitted results for the Rietveld refinement from the XRD patterns of CaMnO$_3$ and Ca$_3$Co$_4$O$_9$, and their corresponding crystal structure. **B** HAADF-STEM image of CaMnO$_3$, the inset denotes the corresponding FFT pattern of STEM image. **C** Atomic-level HAADF-STEM image of Ca3Co4O9. **D** The electric conductivity (σ) and thermal conductivity (*k*), **e** Seebeck coefficient (S) and the calculated power factor (PF) of CaMnO$_3$ and Ca$_3$Co$_4$O$_9$.

Benefiting from the distinct structural property, $CaMnO_3$ and $Ca_3Co_4O_9$ have been studied as promising thermoelectric oxides due to their low thermal conductivity (k), high Seebeck co-efficiency (S) and electric conductivity (σ), and the resulted satisfying power factor (PF = $S^2\sigma$).[22, 25, 26] The two samples were pre-pressed into pellets and be sintered by spark plasma sintering (SPS) technique for thermoelectric characterizations. The temperature dependence of electrical conductivity of $Ca_3Co_4O_9$ shows typical semiconducting behavior during the entire temperature range ($d\sigma/dT > 0$), while the $CaMnO_3$ changed from semiconducting property to metallic with the increase of temperature (Fig. 2d). The total thermal conductivity (κ) of $CaMnO_3$ is found to decrease with increasing temperature, and the κ value of $Ca_3Co_4O_9$ is relatively stable (Fig. 2d). The Seebeck coefficient (S) for $Ca_3Co_4O_9$ becomes larger with increasing temperature, which is typical of semiconducting behavior and hole carriers of the P type $Ca_3Co_4O_9$ (Fig. 2e). Meanwhile, the temperature dependence of S for $CaMnO_3$ is negative, indicating the N-type semiconducting property and the main carriers are electrons (Fig. 2e). The power factor (PF = $S^2\sigma$) of $Ca_3Co_4O_9$ increased much faster than that of $CaMnO_3$ and reached 340 $\mu W\ m^{-1}\ K^{-2}$ at 870 K (Fig. 2e). The dimensionless figure-of-merit (ZT = $\sigma S^2 T/\kappa$) of $CaMnO_3$ and $Ca_3Co_4O_9$ increased with the increase of temperature and reached the top values at the highest temperature (Supplementary Fig. 5). Benefiting from the optimal structural and thermoelectrical property of $CaMnO_3$ and $Ca_3Co_4O_9$, the thermal gradient generated Seebeck voltage and the migration of carriers from hot side to cold side are anticipated to initiate and promote the electrocatalytic activity of the bi-air-electrodes and further enhance the energy efficiency of ZABs.

Electrochemical performance of the air electrodes. To put the proposal into practice, we designed the chamber reactor as illustrated in Supplementary Fig. 6a-b. The reaction chamber was placed on a heating platform and the temperature could be tuned from room temperature to 300 °C. The P- and N-type electrodes were stuck at the bottom of the reactor. The temperature on the hot surface (T_h) of the sample is equal to the bottom floor of the reactor. To precisely control the temperature gradient of the electrodes, the

flow rate of the electrolyte was kept at a steady rate to maintain the cold surface (T_c) of the electrodes at room temperature. The Seebeck voltage generated from thermoelectric (TE) effect can be controlled by tunning the temperature gradient (ΔT). We firstly studied the OER performance of $Ca_3Co_4O_9$ at different temperature gradients. As shown in the linear sweep voltammetry (LSV) curves in Fig. 3a, the OER overpotential decreased significantly from 407 to 306 mV (10 mA cm^{-2}) with the ΔT values increased from 0 to 200 °C. The corresponding Tafel slopes (Fig. 3b) were also decreased from 268 mV dec^{-1} to 63 mV dec^{-1}, demonstrating the OER catalytic kinetics of $Ca_3Co_4O_9$ was optimized at larger ΔT state. Then, we tested the Seebeck voltages of the electrodes at different ΔT. As shown in Fig. 3c and Supplementary Fig. 7-9, the experimental Seebeck voltages that generated from TE effect for $CaMnO_3$, $Ca_3Co_4O_9$, and the series connected $CaMnO_3 + Ca_3Co_4O_9$ are consistent with the theoretical results. As analyzed in Supplementary Fig. 10, the tested Seebeck voltages for $Ca_3Co_4O_9$ are 0, 6.8, 11.8, 14.8, 21.3 and 29.1 mV, but the corresponding variation of the OER overpotential are 0, 15.0, 51.0, 69.0, and 101.0 mV, which are much larger than the generated Seebeck voltages. These results suggest that the enhanced OER performance should not only originating from the thermally-generated Seebeck voltage, but mainly from the enhancement of the intrinsic catalytic activity of the electrodes especially at larger ΔT state. The turnover frequencies (TOFs) of $Ca_3Co_4O_9$ were calculated and the relationship between the TOFs and at ΔT/Seebeck voltages was established (Fig. 3d). The results show that the TOF values increased faster especially at larger ΔT states with higher Seebeck voltages, demonstrating the OER catalytic activity and kinetics of the electrodes were well enhanced at higher temperature gradient. Moreover, the ORR performance of $CaMnO_3$ shows similar enhancing tendency with the increase of ΔT values (Fig. 3e). The potential at 0.1 mA cm^{-2} increased from 0.72 V to 0.81 V (vs. RHE) when the ΔT increased from 0 °C to 200 °C. In addition, the fitted Koutecky-Levich (K-L) plots (Fig. 3f) based on the rotating-ring disk electrode (RRDE) results (Supplementary Fig. 11) show that the $CaMnO_3$ possesses a quasi-4e$^-$ pathway for ORR catalysis, which is recognized as the first-order reaction kinetics for oxygen reduction process. The enhanced OER and ORR performance of $Ca_3Co_4O_9$ and $CaMnO_3$ could

be due to the accumulation of the carriers (charge/hole) on the cold surface of the electrodes especially at higher temperature gradient. More carriers would be generated at larger ΔT state and transferred from hot side to cold surface of the electrodes, and thus changing the electronic structure and the catalytic activity of the active sites. The deeply enhancing mechanism was unveiled using the density functional theory (DFT) calculations.
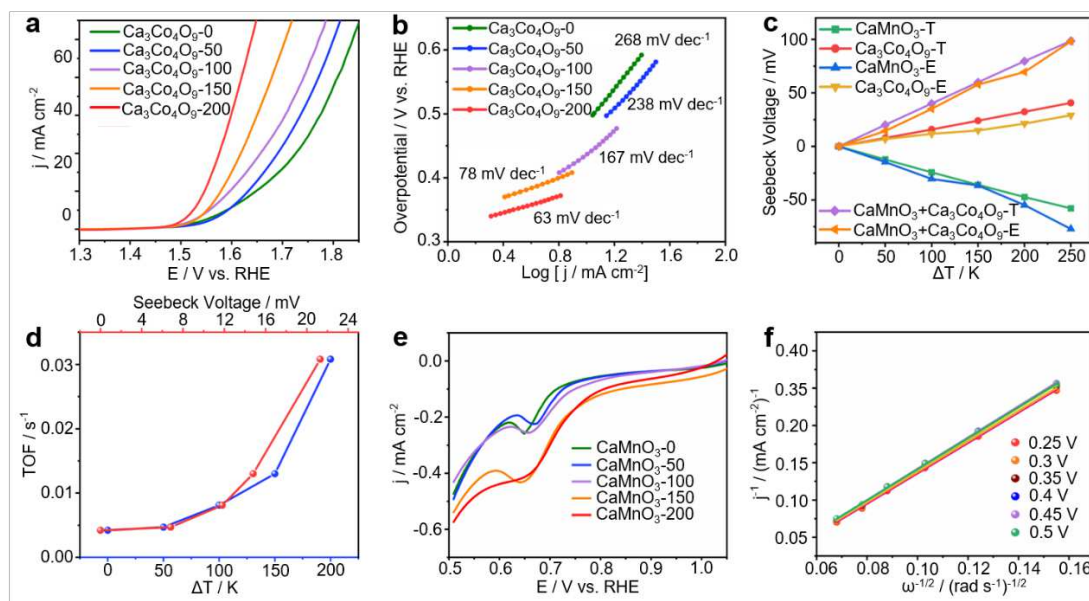

Fig. 3 Electrochemical performance of the air electrodes. **a** The electrocatalytic OER polarization curves of $Ca_3Co_4O_9$ that tested at different ΔT states in 1.0 M KOH. **b** The corresponding OER Tafel plots of $Ca_3Co_4O_9$. **c** Theoretical and experimental Seebeck voltages as functions of ΔT states for $CaMnO_3$, $Ca_3Co_4O_9$, and the series connected $CaMnO_3 + Ca_3Co_4O_9$. **d** The TOF values of $Ca_3Co_4O_9$ at 450 mV overpotential corresponding to different ΔT values and Seebeck voltages. **e** The direct electrocatalytic ORR polarization curves of $CaMnO_3$ at different ΔT states in 0.1 M KOH. **f** The fitted K–L plots of $CaMnO_3$ based on the LSV curves at different potentials.

Theoretical calculations. Computational calculations based on DFT were performed to better illustrate the mechanism of thermoelectricity enhancing electrocatalysis. To keep consistent with the structural and thermoelectrical results, layered $Ca_3Co_4O_9$ model with [020] lattice plane exposure was established and the inner electric field (1.5 eV/Å) was added to simulate the thermoelectric Seebeck voltage (Fig. 4a-b). The atoms were numbered for calculating the Bader charge variation (Supplementary Fig. 12). As

calculated in Fig. 4c-d and Supplementary Fig. 13, the Bader charge around the surface atoms of Ca, Co, and O in $Ca_3Co_4O_9$ decreased while it was increased around the atoms in the inner layer, indicating the extra electric field would trigger the migration of holes from inner to the surface and thus oxidized the surface atoms. On the contrary, however, the Bader charge around the surface atoms of Ca, Mn, and O in $CaMnO_3$ increased and thus their valence states decreased due to the accumulation of electrons (Supplementary Fig. 14-16). The accumulation of carriers ($h^.$ for $Ca_3Co_4O_9$ and e^- for $CaMnO_3$) would change the band structure, work function, and fermi level of the thermoelectrocatalysts, thus potentially influence the catalytic activity of the thermoelectrocatalysts. As shown in Supplementary Fig. 17, more band structure become straight and less intersection can be observed for $Ca_3Co_4O_9$ when adding the extra electric field. Moreover, although the symmetry point in the Brillouin region has changed, it is still a direct band gap semiconductor. These results suggest that the conductivity of pristine $Ca_3Co_4O_9$ ($Ca_3Co_4O_9$-P) and $Ca_3Co_4O_9$ were obviously enhanced by adding an extra electric field ($Ca_3Co_4O_9$-E), which is significantly important for optimizing the OER performance.

Furthermore, we calculated the free energy diagrams of $Ca_3Co_4O_9$ for OER and $CaMnO_3$ for ORR before and after adding the electric field. As shown in Supplementary Fig. 18-19, the intermediates of *OOH, *OH and *O were all energetically favorable to adsorb on the metallic sites of Co in $Ca_3Co_4O_9$ and Mn in $CaMnO_3$ irregardless of the presence of the electric field. For both $Ca_3Co_4O_9$-P and $Ca_3Co_4O_9$-E (Fig. 4e), the rate-limiting step (RLS) corresponds to the deprotonation of OH* to O* species. The energy barrier values for the RLS of $Ca_3Co_4O_9$-E is 1.92 eV, which is much smaller than that of $Ca_3Co_4O_9$-P (2.06 eV), pointing out the importance of the added electric field for reducing the OER barrier and accelerating the reaction kinetic of $Ca_3Co_4O_9$. In addition, for the ORR process, the $CaMnO_3$ with extra electric field ($CaMnO_3$-E) displays exothermic downhill reaction for the four catalytic steps (Fig. 4f) and the four steps would occur spontaneously. However, the pristine $CaMnO_3$ ($CaMnO_3$-P) exhibits an uphill reaction for the transformation from OH^* to OH^- with tough energy barrier of 0.34 eV. The calculation results suggest that the added extra electric field could

obviously modulate the electronic states of catalytic sites in $Ca_3Co_4O_9$ and $CaMnO_3$, and thus accelerating the catalytic kinetics for OER and ORR process.
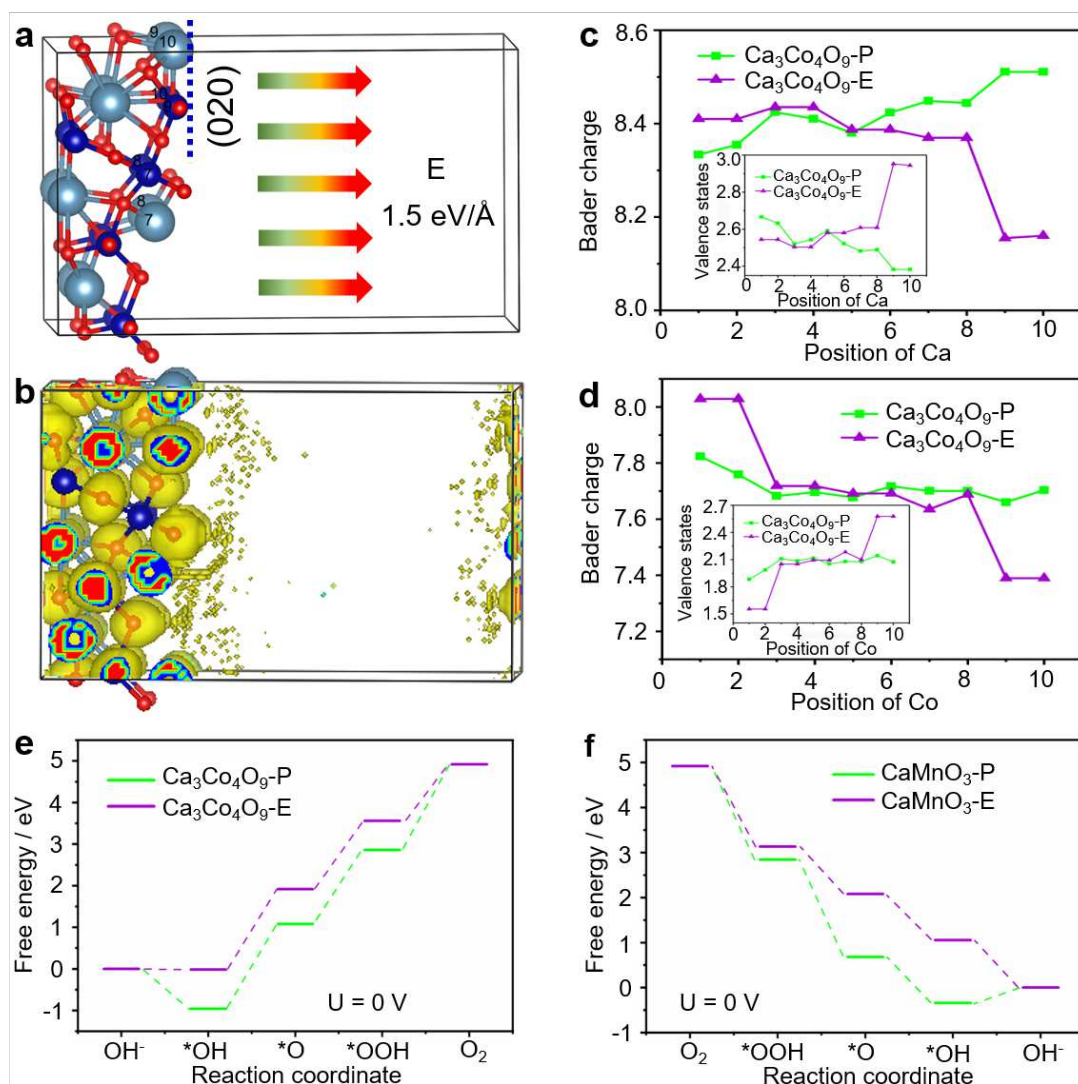

Fig. 4 Theoretical calculations. **a** Parallel perspective about layered $Ca_3Co_4O_9$ model with [020] lattice plane exposure, and the extra electric field (1.5 eV/Å) was added. **b** Corresponding Mulligan charge distribution of $Ca_3Co_4O_9$ with the extra electric field. **c** Bader charge value of Ca, **d** Co atoms at different positions in the primary $Ca_3Co_4O_9$ and electric field-applied $Ca_3Co_4O_9$, inset shows the corresponding valence states. **e** Free energy diagrams for the OER of $Ca_3Co_4O_9$, **f** $CaMnO_3$ before and after adding extra electric field. (The ball in the model: blue is Ca, gray is Co, red is O)

Practical application of the breathing Zn-air batteries. The efficient thermoelectric-enhancement towards the OER and ORR performance of $Ca_3Co_4O_9$ and $CaMnO_3$ inspired us to develop breathing ZABs using the two thermoelectrocatalysts as bi-air-

electrodes. The structure of the model and photograph of breathing ZAB is shown in Supplementary Fig. 20. The $Ca_3Co_4O_9$ and $CaMnO_3$ electrodes were mounted on the heating platform and the valve could be controlled for connection to $Ca_3Co_4O_9$ for discharging and to $CaMnO_3$ for charging. The mixture of 6.0 M KOH and 0.2 M $ZnCl_2$ was used as electrolyte and was cooled to keep at room temperature. The charging and discharging polarization curves of the breathing ZAB at increasing ΔT states were shown in Fig. 5a. Benefiting from the thermoelectric effect, both the charging and discharging curves could be obviously optimized especially at higher ΔT state. The discharge power density was improved from 33.5 to 100.4 mW cm^{-2} with the ΔT values increased from 0 to 200 °C (Fig. 5b). Moreover, the cycling curves at 10 mA cm^{-2} show that the charging potential reduced from 2.08 V to 1.97 V, and the discharging potential was increased from 1.22 V to 1.34 V when the ΔT value increased from 0 to 200 °C (Fig. 5c). The discharge/charge voltage gap for the breathing ZAB decreased from 0.86 V to 0.63 V and the energy efficiency increased from 58.6% to 68.1% (Fig. 5d), which set a new record for the rechargeable ZABs (Supplementary Table 3). In addition, the XRD patterns (Supplementary Fig. 21) show that the $Ca_3Co_4O_9$ and $CaMnO_3$ have no variation after the heating and cycling process, thus ensuring the thermal stability and cycling durability of Zn-air battery. Based on the above experimental and theoretical results, the battery performance improvement should be benefiting from both the Seebeck voltage that generated from the thermoelectric effect and the enhancing intrinsic activity of the active sites in the electrodes.
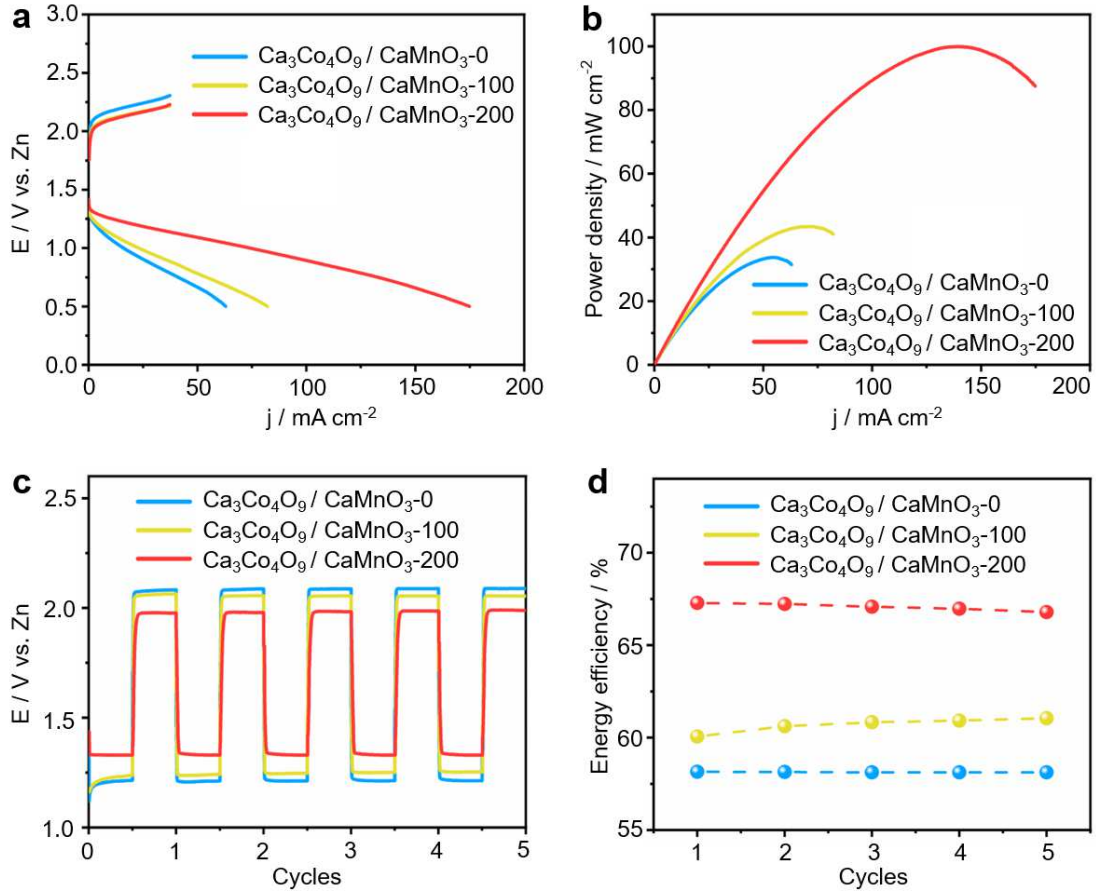
Fig. 5 Battery performance of breathing Zn-air batteries. **a** The charging and discharging polarization curves of the breathing ZABs at the ΔT values of 0, 100 and 200 ℃. **b** The corresponding discharging power density of breathing ZAB at different ΔT states. **c** The cycling performance of breathing ZABs at 10 mA cm^{-2} with ΔT values of 0, 100 and 200 ℃. **d** The round-trip energy efficiency of breathing ZABs at 10 mA cm^{-2} with ΔT values of 0, 100 and 200 ℃.

3. Discussion.

In summary, we designed and developed a breathing ZAB using P-type $Ca_3Co_4O_9$ and N-type $CaMnO_3$ as thermoelectrocatalysts in the bi-air electrode configuration. The $Ca_3Co_4O_9$ and $CaMnO_3$ were physically separated but in-series connected and were employed as OER and ORR electrodes for charging and discharging, respectively. The Seebeck voltages generated from $Ca_3Co_4O_9$ and $CaMnO_3$ under certain temperature gradients could synergistically compensate part of the OER and ORR overpotentials. The electronic state and band energy structure of the air electrodes could also be modulated due to the accumulation of carriers on the could surface of the electrodes,

and thus further optimizing the intrinsic OER and ORR activity. Benefiting from the thermoelectric effect of the air electrodes, the OER and ORR overpotentials were enhanced by 101 and 90 mV at ΔT value of 200 °C. The breathing ZABs display a remarkable energy efficiency of 68.1% with well stability.

Supporting Information.

Experimental details; photographs, battery performance, SEM and TEM images, XPS spectra, and calculation results of $Ca_3Co_4O_9$, $CaMnO_3$, and ZABs.

Declaration of Competing Interest

The authors declare that they have no known competing financial interests or personal relationships that could have appeared to influence the work reported in this paper.

Authorship contribution statement

Xuerong Zheng: Methodology, Formal analysis, Writing – original draft, Writing – review & editing. **Yanhui Cao:** Investigation, Methodology. **Xiaopeng Han:** Resources. **Zhao Zhang:** Investigation. **Menghan Zhao:** Investigation. **Jihong Li:** Methodology. **Yang Wang:** Characterization. **Haozhi Wang:** Theoretical calculation. **Jiajun Wang:** Investigation. **Yuesheng Wang:** Conceptualization, writing – review & editing. **Yida Deng:** Conceptualization and Resources. **Li Zhang:** Resources. **Wenbin Hu:** Writing – review

Data availability

The data that support the findings of this study are available from the corresponding author upon reasonable request.

References

[1] Li, C. S. et al. Current progress on rechargeable magnesium-air battery. *Adv. Energy*

Mater. **7**, 1700869 (2017).

[2] Lu, Q. et al. Encapsulating cobalt nanoparticles in interconnected N-doped hollow carbon nanofibers with enriched CoNC moiety for enhanced oxygen electrocatalysis in Zn-air batteries. *Adv. Sci.* **8**, 2101438 (2021).

[3] Wu, S. et al. Hybrid high-concentration electrolyte significantly strengthens the practicability of alkaline aluminum-air battery. *Energy Storage Materials* **31**, 310-317 (2020).

[4] Zheng, X. et al. Identifying dense $NiSe_2$/$CoSe_2$ heterointerfaces coupled with surface high-valence bimetallic sites for synergistically enhanced oxygen electrocatalysis. *Adv. Mater.* **32**, 2000607 (2020).

[5] Han, X. et al. Identifying the activation of bimetallic sites in $NiCo_2S_4$@g-C_3N_4-CNT hybrid electrocatalysts for synergistic oxygen reduction and evolution. *Adv. Mater.* **31**, 1808281 (2019).

[6] Zheng, X. et al. Rational design and spontaneous sulfurization of NiCo-(oxy)hydroxysulfides nanosheets with modulated local electronic configuration for enhancing oxygen electrocatalysis. *Adv. Energy Mater.* **12**, 2103275 (2022).

[7] Li, Y. et al. Advanced zinc-air batteries based on high-performance hybrid electrocatalysts. *Nat. Commun.* **4**, 1805 (2013).

[8] Liu, X. et al. A stable bifunctional catalyst for rechargeable zinc-air batteries: iron-cobalt nanoparticles embedded in a nitrogen-doped 3D carbon matrix. *Angew. Chem. Int. Ed.* **57**, 16166-16170 (2018).

[9] Xu, Y. et al. 2D nitrogen-doped carbon nanotubes/graphene hybrid as bifunctional oxygen electrocatalyst for long-life rechargeable Zn-air batteries. *Adv. Funct. Mater.* **30**, 1906081 (2019).

[10] An, L. et al. Interfacial defect engineering for improved portable zinc-air batteries with a broad working temperature. *Angew. Chem. Int. Ed.* **58**, 9459-9463 (2019).

[11] Tang, C. et al. Defect engineering toward atomic Co-N_x-C in hierarchical graphene for rechargeable flexible solid Zn-air batteries. *Adv. Mater.* **29**, 1703185 (2017).

[12] Zheng, X. et al. Engineering interface and oxygen vacancies of $Ni_xCo_{1-x}Se_2$ to boost oxygen catalysis for flexible Zn-air batteries. *ACS Appl. Mater. Interfaces*

11, 27964-27972 (2019).

[13] Zheng, X. et al. Bimetallic metal-organic-framework/reduced graphene oxide composites as bifunctional electrocatalysts for rechargeable Zn-air batteries. *ACS Appl. Mater. Interfaces* **11**, 15662-15669 (2019).

[14] Wang, J. et al. Developing indium-based ternary spinel selenides for efficient solid flexible Zn-air batteries and water splitting. *ACS Appl. Mater. Interfaces* **12**, 8115-8123 (2020).

[15] Wang, Q. et al. Pyridinic-N-dominated doped defective graphene as a superior oxygen electrocatalyst for ultrahigh-energy-density Zn-air batteries. *ACS Energy Lett.* **3**, 1183-1191 (2018).

[16] Wang, Q. et al. NiFe layered double hydroxide nanoparticles on Co, N-codoped carbon nanoframes as efficient bifunctional catalysts for rechargeable zinc-air batteries. *Adv. Energy Mater.* **7**, 1700467 (2017).

[17] Qu, J. et al. Direct thermal enhancement of hydrogen evolution reaction of on-chip monolayer MoS_2. *ACS Nano* **16**, 2921-2927 (2022).

[18] Fan, X. et al. From theory to experiment: cascading of thermocatalysis and electrolysis in oxygen evolution reactions. *ACS Energy Lett.* **7**, 343-348 (2022).

[19] Yan J. et al. Direct magnetic reinforcement of electrocatalytic ORR/OER with electromagnetic induction of magnetic catalysts. *Adv. Mater.* **33**, 2007525 (2021).

[20] Zhang, J. et al. A metal-free bifunctional electrocatalyst for oxygen reduction and oxygen evolution reactions. *Nat. Nanotech.* **10**, 444-452 (2015).

[21] Chen, P. et al. Atomically dispersed iron-nitrogen species as electrocatalysts for bifunctional oxygen evolution and reduction reactions. *Angew. Chem. Int. Ed.* **56**, 610-614 (2017).

[22] Sharifi, T. et al. Thermoelectricity enhanced electrocatalysis. *Nano Lett.* **17**, 7908-7913 (2017).

[23] Mohammed, M. A., Uday, M. B. & Izman, S. Effects of calcination temperature and time on the $Ca_3Co_4O_9$ purity when synthesized using starch-assisted sol–gel combustion method. *J. Adv. Ceram.* **9**, 162-172 (2020).

[24] Lin, X. et al. An efficient family of misfit-layered calcium cobalt oxide catalyst for

oxygen evolution reaction. *Adv. Mater. Interfaces* **5**, 1801281 (2018).

[25] Achour, A. et al. In situ tuning of catalytic activity by thermoelectric effect for ethylene oxidation. *ACS Catal.* **8**, 10164-10172 (2018).

[26] Achour, A. et al. Tuning of catalytic activity by thermoelectric materials for carbon dioxide hydrogenation. *Adv. Energy Mater.* **8**, 1701430 (2018).
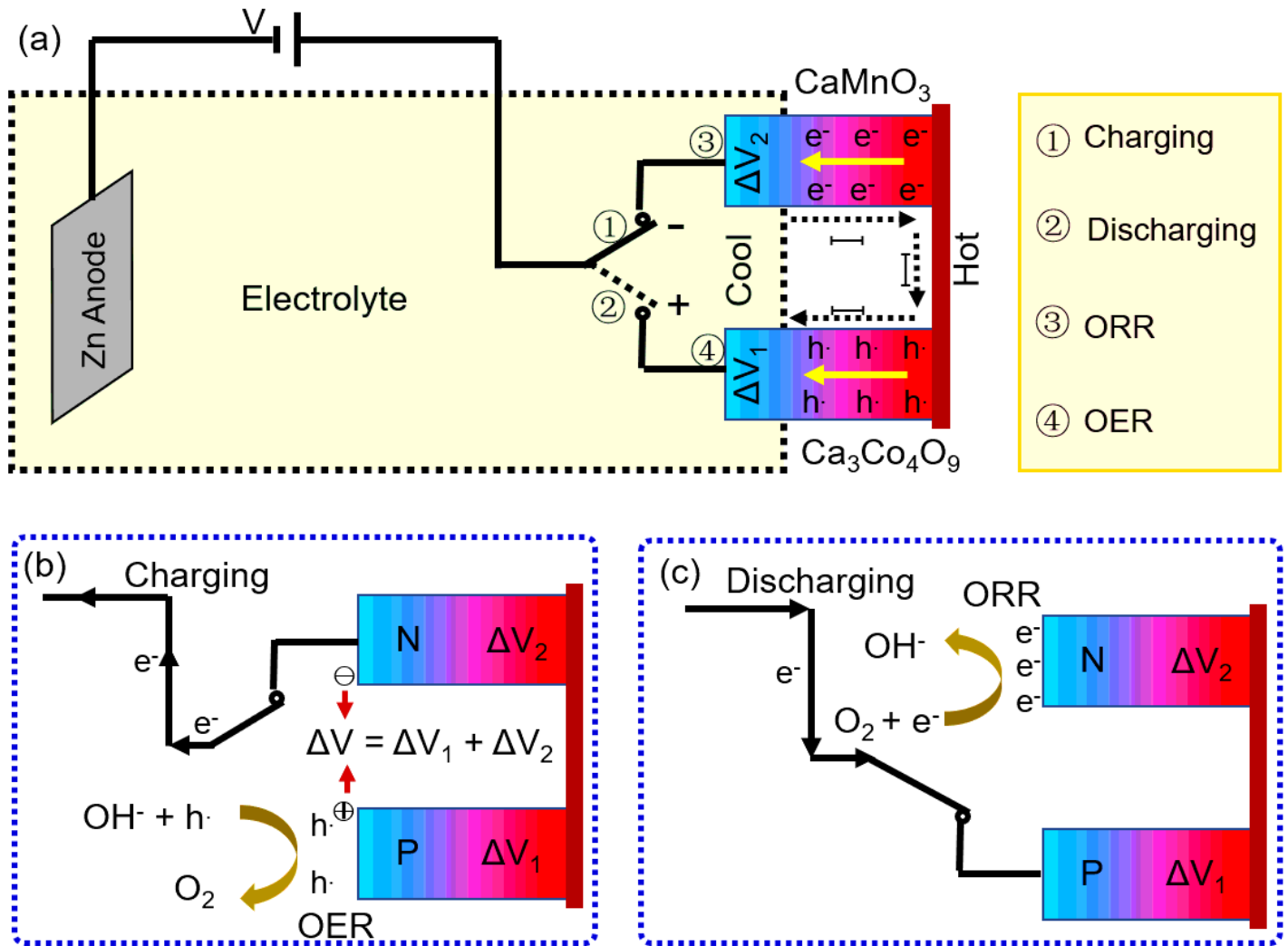
Figures

Figure 1

Designing mechanism of breathing ZABs. **a** Schematic illustration of the breathing ZAB with thermoelectric-promoted air-breathing configuration. The detail illustration of **b** charging and **c** discharging process in the air-breathing configuration.
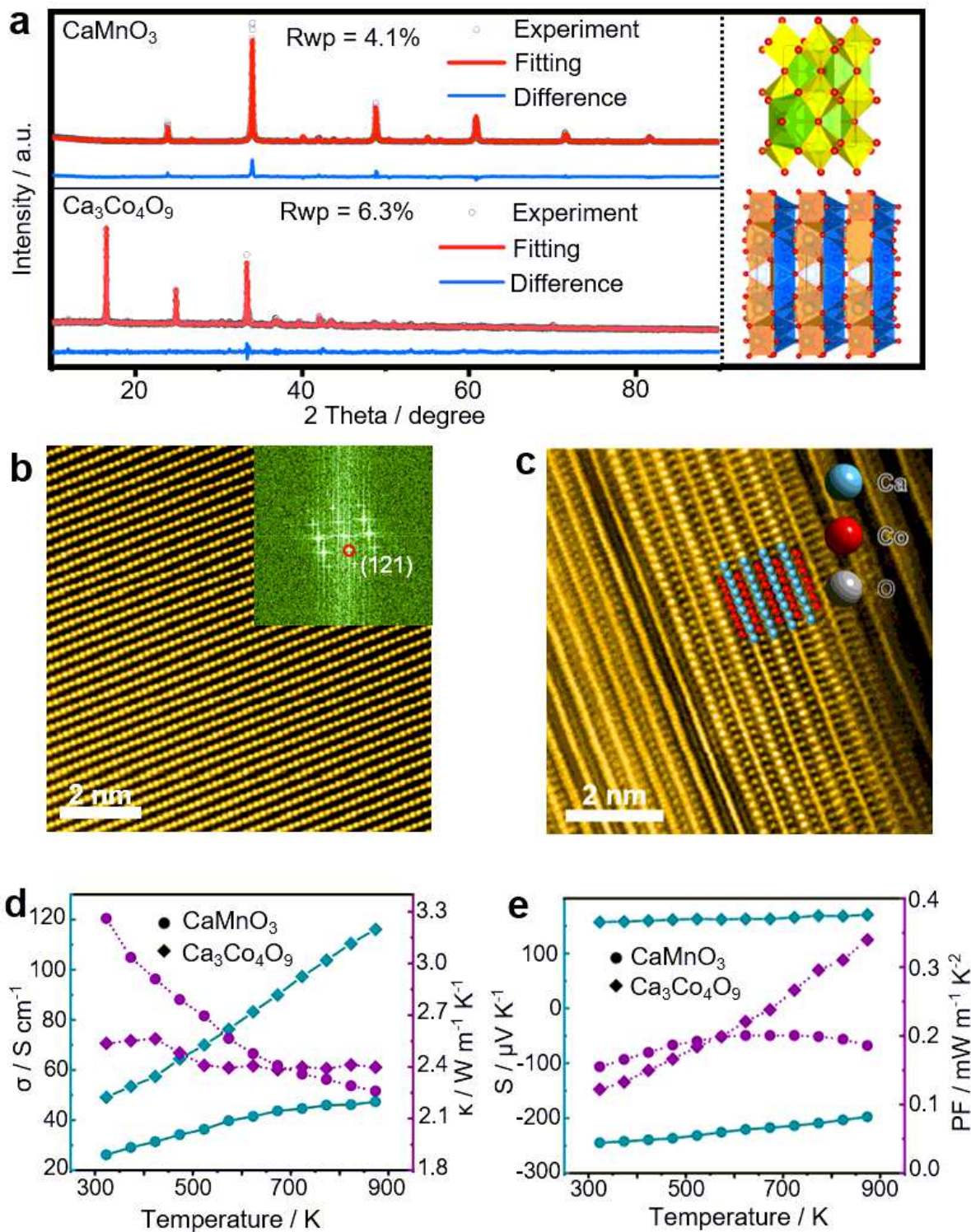
Figure 2

Characterizations of thermoelectrocatalysts. **A** Characterized, calculated, and fitted results for the Rietveld refinement from the XRD patterns of CaMnO3and Ca3Co4O9, and their corresponding crystal structure. **B** HAADF-STEM image of CaMnO3, the inset denotes the corresponding FFT pattern of STEM image. **C** Atomic-level HAADF-STEM image of Ca3Co4O9. **D** The electric conductivity (σ) and thermal conductivity (k), **e** Seebeck coefficient (S) and the calculated power factor (PF) of CaMnO3 and Ca3Co4O9.

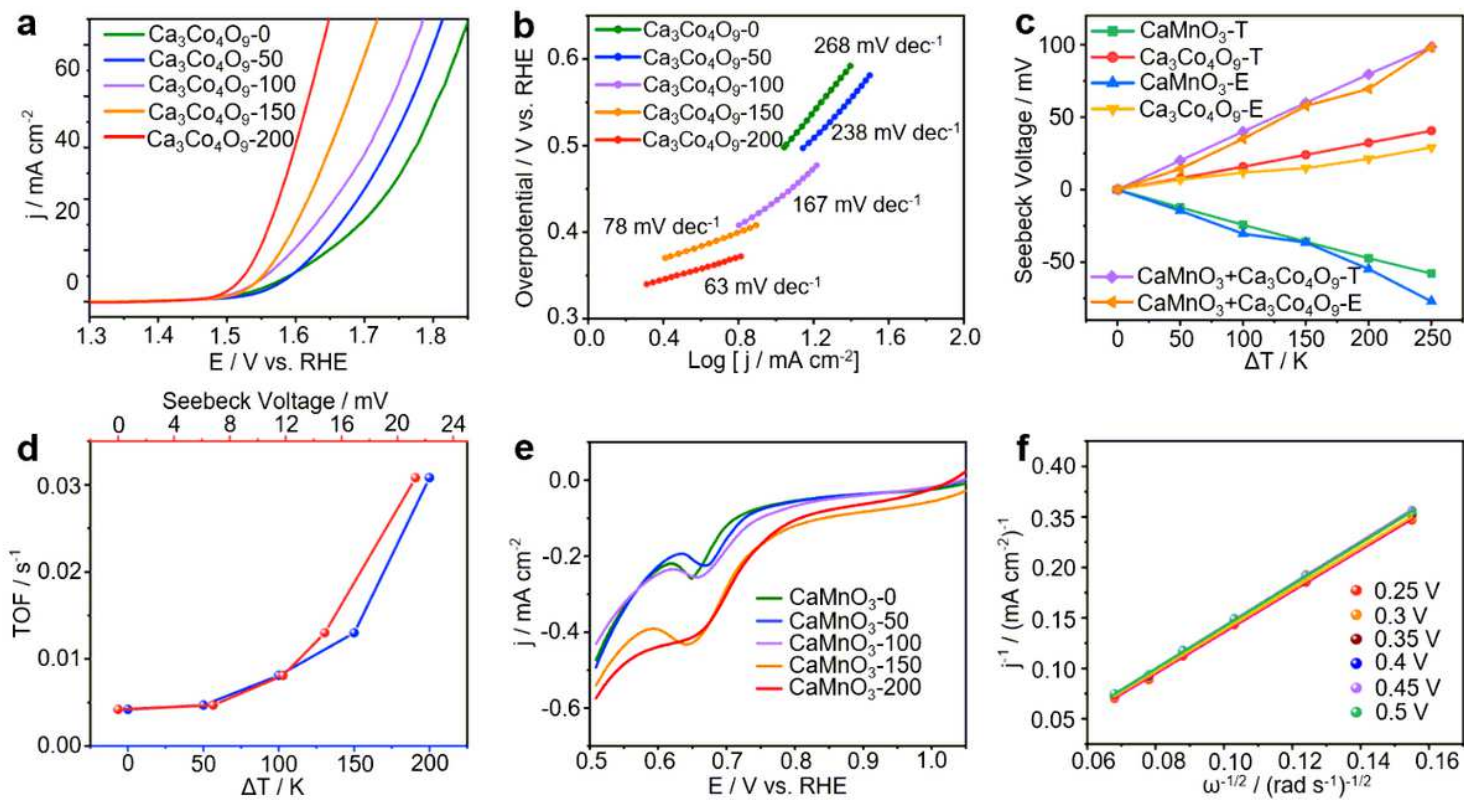**Figure 3**

Electrochemical performance of the air electrodes. **a** The electrocatalytic OER polarization curves of Ca3Co4O9that tested at different ΔT states in 1.0 M KOH. **b** The corresponding OER Tafel plots of Ca3Co4O9. **c** Theoretical and experimental Seebeck voltages as functions of ΔT states for CaMnO3, Ca3Co4O9, and the series connected CaMnO3+ Ca3Co4O9. **d** The TOF values of Ca3Co4O9at 450 mV overpotential corresponding to different ΔT values and Seebeck voltages. **e** The direct electrocatalytic ORR polarization curves of CaMnO3at different ΔT states in 0.1 M KOH. **f** The fitted K−L plots of CaMnO3based on the LSV curves at different potentials.

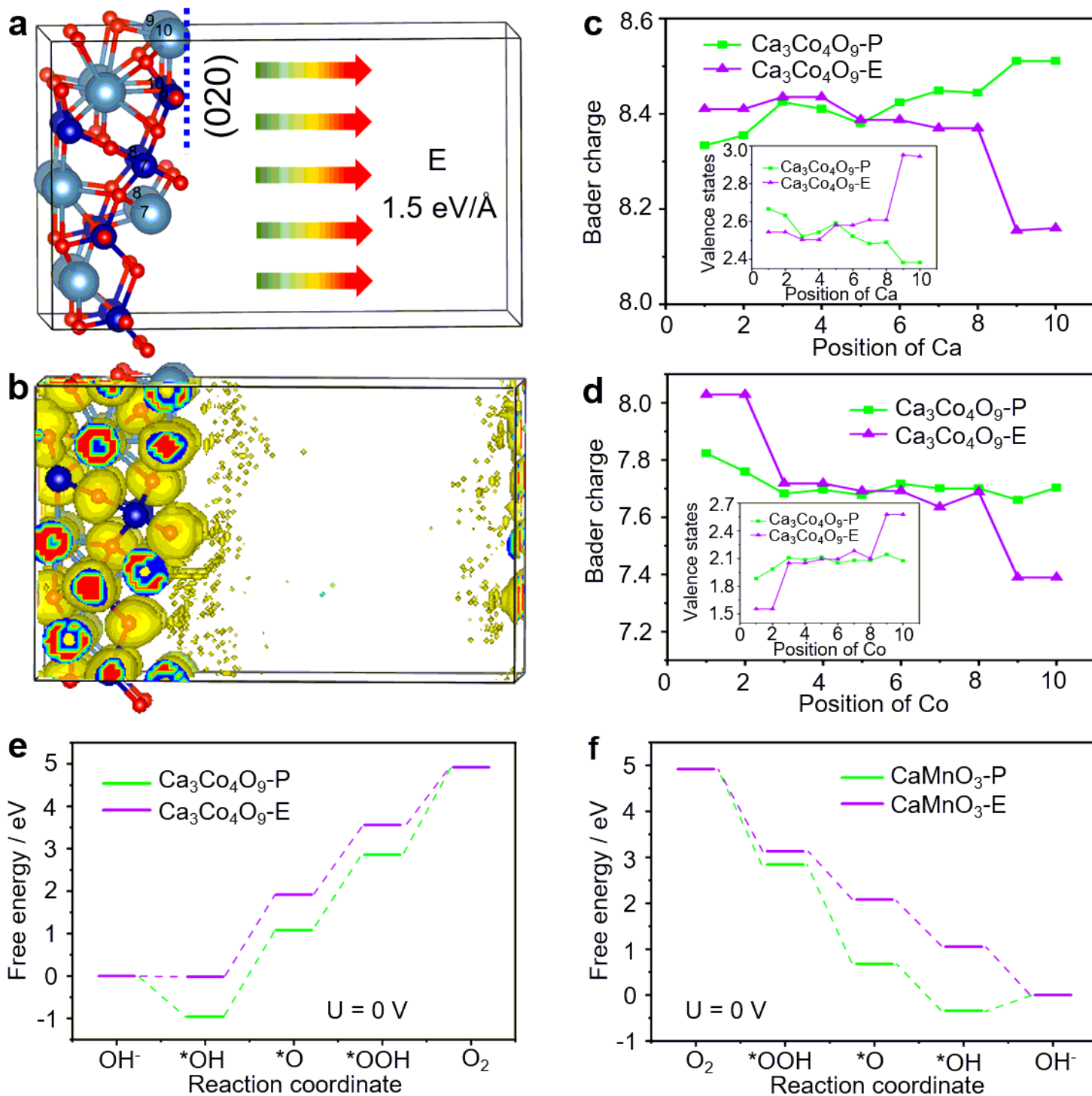**Figure 4**

Theoretical calculations. **a** Parallel perspective about layered Ca3Co4O9model with [020] lattice plane exposure, and the extra electric field (1.5 eV/Å) was added. **b** Corresponding Mulligan charge distribution of Ca3Co4O9 with the extra electric field. **c** Bader charge value of Ca, **d** Co atoms at different positions in the primary Ca3Co4O9and electric field-applied Ca3Co4O9, inset shows the corresponding valence states. **e** Free energy diagrams for the OER of Ca3Co4O9, **f** CaMnO3before and after adding extra electric field. (The ball in the model: blue is Ca, gray is Co, red is O)
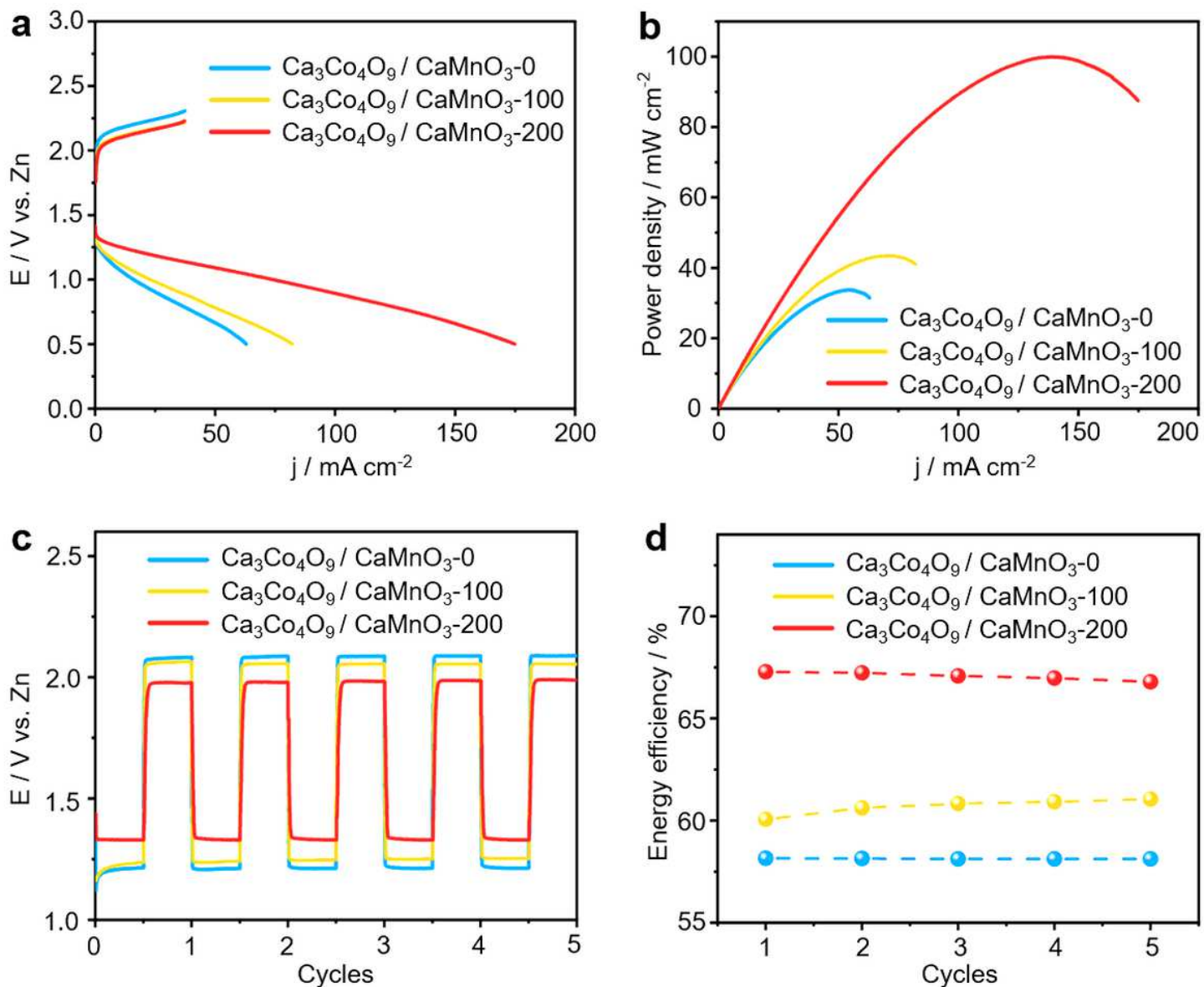
Figure 5

Battery performance of breathing Zn-air batteries. **a** The charging and discharging polarization curves of the breathing ZABs at the ΔT values of 0, 100 and 200 . **b** The corresponding discharging power density of breathing ZAB at different ΔT states. **c** The cycling performance of breathing ZABs at 10 mA cm-2 with ΔT values of 0, 100 and 200 . **d** The round-trip energy efficiency of breathing ZABs at 10 mA cm-2 with ΔT values of 0, 100 and 200 .

Supplementary Files

This is a list of supplementary files associated with this preprint. Click to download.

- SI.docx